Chapter 22
A Microstructurally Based Multi-Scale Constitutive Model of Active Myocardial Mechanics

Adarsh Krishnamurthy, Benjamin Coppola, Jared Tangney, Roy C.P. Kerckhoffs, Jeffrey H. Omens, and Andrew D. McCulloch

Abstract Contraction of cardiac muscle cells provides the work for ventricular pumping. The primary component of this contractile stress development in myocardium acts along the axis of the myofilaments; however, there may be a component directed transversely as well. Biaxial testing of tonically activated cardiac tissue has shown that myocardium can generate active stresses in the transverse direction that are as high as 50 % of those developed along the fiber axis. The microstructural basis for this is not clear. We hypothesized that transverse active stresses are generated at the crossbridge and myofilament lattice scales and transmitted via the myocardial laminar sheets as plane stress objects. To test this hypothesis, we developed a multi-scale constitutive model accounting for crossbridge and myofilament lattice structures as well as multicellular myofiber and sheet angle dispersions. Integrating these properties in a finite element model of an actively contracting myocardial tissue slice suggested that these mechanisms may be sufficient to explain the results of biaxial tests in contracted myocardium.

22.1 Introduction

It is well known that cardiac muscle fibers develop active force along the longitudinal myofibril axis of the myocyte. Both the actin and myosin filaments are oriented along the myofibrils, and it is their relative motions that lead to muscle fiber shortening and thickening. However, the acto-myosin crossbridges are not oriented

Invited Book Chapter in "Structure-Based Mechanics of Tissues and Organs: A Tribute to Yoram Lanir"

A. Krishnamurthy (✉) • B. Coppola • J. Tangney • R.C.P. Kerckhoffs • J.H. Omens • A.D. McCulloch
AQ1 Departments of Bioengineering and Medicine, Cardiac Biomedical Science and Engineering Center, University of California, San Diego, CA, USA

G.S. Kassab, M.S. Sacks (eds.), *Structure-Based Mechanics of Tissues and Organs*,
DOI 10.1007/978-1-4899-7630-7_22

parallel to the myofilaments. Structural studies suggest that the actin-binding region of myosin when the crossbridge is in the strongly bound state forms an acute angle between the binding site on actin and the backbone of the thick filament (Huxley 1985; Huxley and Kress 1985). Theoretical analysis suggests that this may give rise to a significant component of force radial to the myofilament long axis (Schoenberg 1980a, b; Zahalak 1996). The magnitude of this radial component likely depends on this binding angle, the filament spacing, and the sarcomere length. In biaxial tests of an isolated myocardial tissue preparation, Lin and Yin (1998) showed that the multicellular myocardium can generate significant systolic transverse stresses (greater than 40 % of those in the fiber direction). They concluded that fiber angle variations within the specimens alone would be insufficient to explain transverse stresses of this magnitude, thus implicating an active cellular mechanism for transverse tension generation. Finite element models of the heart have traditionally used uniaxial active stress models (Guccione and McCulloch 1993; Hunter et al. 1998). However, it has been shown that the inclusion of transverse active stress in models of ventricular mechanics significantly improves the agreement between predicted systolic wall strains and experimentally measured deformations in the intact heart (Usyk et al. 2000).

Thus, there is a need for microstructurally derived constitutive models to link crossbridge models of tension development in sarcomeres to tissue-scale models of systolic myocardial wall stress development. Here we consider structural mechanisms at four different scales of myocardial organization of multi-axial systolic stress development and derive a hierarchical multi-scale microstructural model of anisotropic systolic myocardial stress–strain relations. We assume that the input to such a model is a lumped parameter model of calcium-dependent myofilament activation and crossbridge interactions such as Markov model described recently (Campbell et al. 2010). This model in turn could be activated by a model of dynamic myocyte depolarization and excitation–contraction coupling such as the model by Campbell et al. (2009). The twitch tension developed in these models depends on processes at the crossbridge, sarcomere, and whole cell scales. However, we can use the computed tension to derive the force in a single average crossbridge, for the purposes of deriving a microstructural model of three-dimensional myocardial active stresses.

We consider mechanisms at four scales: (1) In the single crossbridge scale, we consider the two-dimensional static equilibrium of a strongly bound crossbridge to resolve the crossbridge stiffness into longitudinal and transverse components, using a similar approach to that proposed by Schoenberg (1980a, b) and accounting for changes in lattice spacing with sarcomere length; (2) At the intracellular scale, we consider the hexagonal arrangements of thick and thin filaments in the organized myofilament lattice to derive how active stresses are developed anisotropically within myocytes; (3) At the multicellular single laminar sheet scale, we integrate these anisotropic stress tensors within a laminar sheet to derive the tissue-scale effects of dispersion of myofibers about the mean fiber orientation (Karlon et al. 1998); and (4) finally we consider the effects of distributions of myocardial laminae and their orientations within the myocardium on orthotropic systolic stress development (LeGrice et al. 1995).

In order to test the resulting multi-scale microstructural constitutive law, we integrated it into a three-dimensional finite element model. The model includes measurements of fiber-sheet distributions in one dog. The stresses developed in the model were then compared with those in the biaxial tests performed in tonically activated rabbit myocardium by Lin and Yin (1998).

22.2 Methods

22.2.1 Histological Measurements

The histological measurements used in the current model were taken from a canine heart used in a previous study in our laboratory (Coppola et al. 2007). All animal studies were performed according to the National Institutes of Health *Guide for the Care and Use of Laboratory Animals*. All protocols were approved by the Animal Subjects Committee of the University of California, San Diego, which is accredited by the American Association for Accreditation of Laboratory Animal Care. An adult mongrel dog was instrumented as described in detail in Coppola et al. (2007). The heart was fixed in situ at end-diastolic pressure with 2.5 % gluteraldehyde and stored in 10 % formalin. The heart was then sectioned for histology as previously described (Ashikaga et al. 2004). These sections are cut perpendicular to the mean fiber direction so that the sheet angle β can be visualized directly. Sheet angles were measured at each transmural depth using the method of Karlon et al. (1998). Ten 10-μm sections were analyzed (50–70 sheet angles per section) for a total of about 600 measurements of the sheet angle, β, across the wall thickness. These sheet angle populations were incorporated into the finite element model.

22.2.2 Crossbridge Mechanics

The static equilibrium of the strongly bound myosin molecule based on a 2D simplification of the model originally proposed by Schoenberg (1980a, b) was used to resolve crossbridge tension into axial and transverse (radial) components. The axial and radial stiffnesses of the structure were then derived and used to compute the resulting axial and radial stresses in the hexagonal sarcomere lattice model.

Tension in the elastic S2 segment is resolved into axial and transverse components using a two-dimensional force and moment balance derived from the geometry shown in Fig. 22.1 and assuming no net moment at the attachment of the S1 head to the thin filament. To derive crossbridge stiffness components, the lattice spacing of the crossbridge model is displaced by a small value and the resulting change in the axial and radial forces is obtained (Fig. 22.1). This change in force is then used

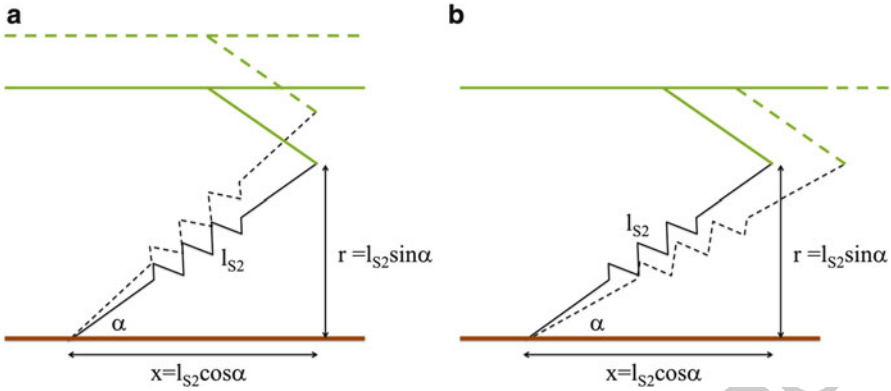

Fig. 22.1 Computing the crossbridge stiffness in the axial and radial direction based on the geometry of the myosin S2 segment. The myosin S2 segment makes an angle α with the thick filament of myosin

to derive the instantaneous stiffnesses in the two directions (Chuang et al. 2012). It can be shown that the transverse to fiber crossbridge stiffness-ratio is

$$\frac{K_t}{K_f} = \frac{l_{S2} - l_0 \cos^2\alpha}{l_{S2} - l_0 \sin^2\alpha} \tag{22.1}$$

where l_{S2} is the length of the S2 segment of the crossbridge, l_0 is the resting length of the crossbridge considering the S2 segment to be a linear spring, and α is the angle between the S2 segment and the thick filament of the myosin molecule.

22.2.3 Lattice Model

A hexagonal lattice model of the sarcomeres was used to derive transverse and axial stresses as a function of the lattice spacing and crossbridge stiffness components. The lateral force interactions in a myofilament lattice due to crossbridge formation between thick and thin filaments can be analyzed in two perpendicular planes: one parallel to the axis of the sarcomeres, and one perpendicular to the axis of the sarcomeres. Figure 22.2a shows the cross-section in this perpendicular plane. We make use of energy conservation in a hexagonal unit cell of width Δ_0 and axial length δ_0 consisting of three pairs of crossbridges as shown in Fig. 22.2b to derive the resultant axial and radial stress components. For this analysis, the three pairs of crossbridges are assumed to be in the same plane.

The complete derivation for the strain analysis is given in Chuang et al. (2012). In terms of the ratio of the transverse to the radial stiffness (K_t/K_f) derived from

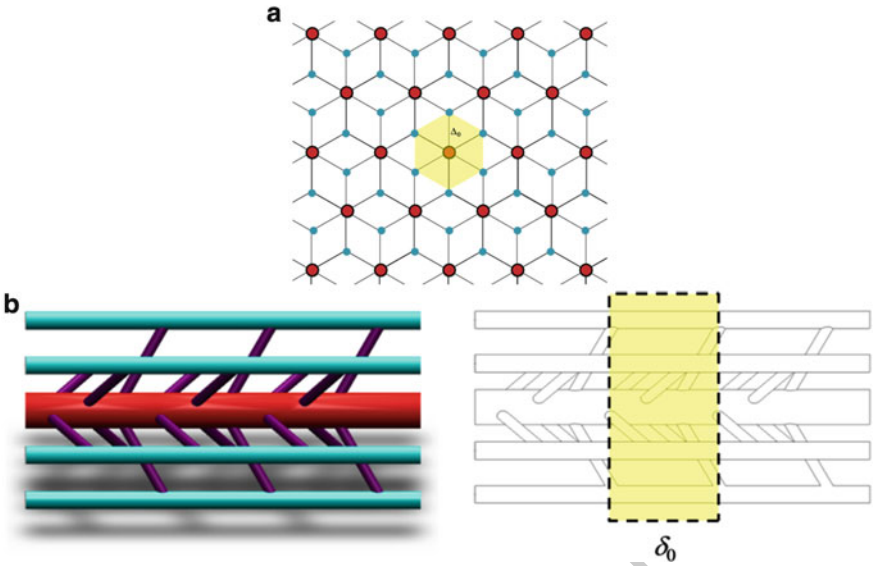

Fig. 22.2 (**a**) Lattice structure showing the cross-section of the thick myosin filaments (*red*) and the thin actin filaments (*blue*) in a 2D view. The section consists of three pairs of crossbridges. A single unit cell used for the analysis with six crossbridges is highlighted in *yellow*. (**b**) Axial view of sarcomeres showing three sets of three pairs of crossbridges spaced 120° apart. The unit cell consisting of three pairs of crossbridges and axial length δ_0 is marked in *yellow*

the crossbridge analysis, the ratio of the stresses in the radial direction to the axial direction derived for the lattice is

$$\nu = \frac{S_t}{S_f} = \frac{1}{2}\left(\frac{\Delta}{\delta_0}\right)\frac{K_t}{K_f} \tag{22.2}$$

22.2.4 Active Systolic Stress

We use the stress ratio derived from the previous section to derive the active stress tensor at the tissue level. At each integration point of the finite element model, the active fiber stress of a myocyte is calculated from the Guccione activation model (Guccione and McCulloch 1993) as a function of sarcomere length and time. From this fiber stress, S_f, we use (22.2) to obtain the transverse stress $S_t = \nu \bullet S_f$ at the single myocyte scale. We assume the resulting myocyte systolic active stress is transversely isotropic. Now considering myocytes distributed within a planar sheet assumed to behave as a plane stress element due to weak sheet-sheet coupling, then

there can be no stress acting in the sheet-normal direction. Therefore, contribution of a single myocyte directed parallel to the mean fiber orientation within a sheet is

$$\boldsymbol{T} = \begin{bmatrix} S_{\mathrm{f}} & 0 & 0 \\ 0 & \nu \cdot S_{\mathrm{f}} & 0 \\ 0 & 0 & 0 \end{bmatrix} \quad \text{with respect to}: \{\mathbf{e}_{\mathrm{f}}, \mathbf{e}_{\mathrm{s}}, \mathbf{e}_{\mathrm{n}}\} \tag{22.3}$$

where $\mathbf{e}_{\mathrm{f}}$ represents the fiber direction, $\mathbf{e}_{\mathrm{s}}$ represents the within-sheet direction, and $\mathbf{e}_{\mathrm{n}}$ represents the cross-sheet direction associated with this individual sheet.

We assume that all myofibers within a sheet are parallel to the plane of the sheet but are distributed with an angular distribution $f(\varphi)$ with respect to the mean fiber direction (see Fig. 22.3a). Taking into account this distribution, the stresses in this single sheet can be obtained by integrating:

$$\boldsymbol{T}_{\text{sheet}} = \int_{-\pi/2}^{\pi/2} \boldsymbol{R}_{\varphi} \cdot \boldsymbol{T} \cdot \boldsymbol{R}_{\varphi}^{T} \cdot f(\varphi) \cdot d\varphi$$
$$\boldsymbol{R}_{\varphi} = \begin{bmatrix} \cos(\varphi) & \sin(\varphi) & 0 \\ -\sin(\varphi) & \cos(\varphi) & 0 \\ 0 & 0 & 1 \end{bmatrix} \quad \text{with respect to}: \{\mathbf{e}_{\mathrm{f}}, \mathbf{e}_{\mathrm{s}}, \mathbf{e}_{\mathrm{n}}\} \tag{22.4}$$

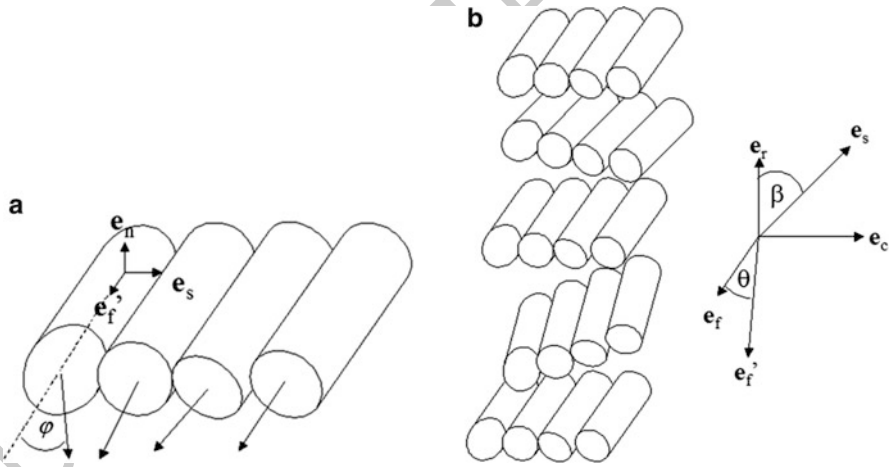

Fig. 22.3 Description of angles in model. (**a**) Schematic representation of a single sheet. $\mathbf{e}_{\mathrm{f}}'$ represents the sheet mean fiber axis, $\mathbf{e}_{\mathrm{s}}$ represents the direction transverse to the fiber direction but within the sheet, and $\mathbf{e}_{\mathrm{n}}$ represents the sheet-normal direction (across the thickness of the sheet). φ represents the deviation of a single myocytes fiber axis relative to the mean fiber axis. φ is measured in the ($\mathbf{e}_{\mathrm{f}}'$, $\mathbf{e}_{\mathrm{s}}$) plane. (**b**) Schematic representation of several sheets. $\mathbf{e}_{\mathrm{f}}$ represents the tissue mean fiber axis, $\mathbf{e}_{\mathrm{r}}$ represents the radial direction, and $\mathbf{e}_{\mathrm{c}}$ is perpendicular to both ($\mathbf{e}_{\mathrm{c}} = \mathbf{e}_{\mathrm{r}} \times \mathbf{e}_{\mathrm{f}}$). Each sheet has a sheet mean fiber axis at an angle θ to the tissue mean fiber axis, in the ($\mathbf{e}_{\mathrm{f}}$, $\mathbf{e}_{\mathrm{r}}$) plane. Each sheet also has an angle β, which is in the ($\mathbf{e}_{\mathrm{c}}$, $\mathbf{e}_{\mathrm{r}}$) plane

where $f(\varphi)$ represents the distribution of φ, which we define to have a mean of zero. $\boldsymbol{T}_{\text{sheet}}$ remains a plane stress, but it is no longer a diagonal tensor in general. In other words, there may be a shear stress component due to the dispersion of $\varphi\varphi$ within the sheet. However, if the distribution is symmetric, the shear terms cancel out making the tensor diagonal.

In the finite element formulation, stresses are integrated at the tissue scale. At this scale, there are many sheets. Each sheet has an orientation associated with it, which can be described as a function of two angles: β, which is the histologically measured sheet angle (Costa et al. 1999) and θ, which is the angle relative to the mean fiber direction (about the sheet direction). For an illustration of these angles, see Fig. 22.3b. Now the stress at the tissue level can be integrated:

$$\boldsymbol{T}_{\text{tissue}} = \iint \boldsymbol{R}_\theta \boldsymbol{R}_\beta \boldsymbol{T}_{\text{sheet}} \boldsymbol{R}_\beta^{\text{T}} \boldsymbol{R}_\theta^{\text{T}} f(\theta) f(\beta)\, d\theta d\beta$$
$$\boldsymbol{R}_\beta = \begin{bmatrix} 1 & 0 & 0 \\ 0 & \sin(\beta) & \cos(\beta) \\ 0 & -\cos(\beta) & \sin(\beta) \end{bmatrix}, \quad \boldsymbol{R}_\theta = \begin{bmatrix} \cos(\theta) & 0 & \sin(\theta) \\ 0 & 1 & 0 \\ -\sin(\theta) & 0 & \cos(\theta) \end{bmatrix} \tag{22.5}$$
$$\text{with respect to}: \{\mathbf{e}_{\text{f}}, \mathbf{e}_{\text{c}}, \mathbf{e}_{\text{r}}\}$$

where $\mathbf{e}_{\text{f}}$ represents the fiber direction, $\mathbf{e}_{\text{r}}$ represents the radial (transmural) direction, and $\mathbf{e}_{\text{c}}$ represents the cross-fiber direction ($\mathbf{e}_{\text{c}} = \mathbf{e}_{\text{r}} \times \mathbf{e}_{\text{f}}$) associated with the bulk tissue; $f(\theta)$ and $f(\beta)$ represent the distributions of θ and β, respectively. Note that the different format of $\mathbf{R}_\beta$ is consistent with Costa's definition (Costa et al. 1999).

The angles φ, θ, and β change through time as the heart deforms. In other words, they are functions of Lagrangian strain ($\mathbf{E}$), as shown in the Appendices 1 and 2. Because these quantities vary through time, the integration has to be performed at each time step of the finite element solver. However, if we assume there is no interaction between the angles, the integration terms can be separated and can be evaluated by evaluating the following definite integrals:

AQ3

$$\begin{aligned} I_{\cos^2\gamma} &= \int_{-\pi/2}^{\pi/2} \cos^2\gamma f(\gamma)\, d\gamma \\ I_{\cos\gamma} &= \int_{-\pi/2}^{\pi/2} \cos\gamma f(\gamma)\, d\gamma \\ I_{\sin^2\gamma} &= \int_{-\pi/2}^{\pi/2} \sin^2\gamma f(\gamma)\, d\gamma \end{aligned} \tag{22.6}$$

where f represents a Von-Mises distribution for the angles and γ represents θ, β, or φ. More details are given in the Appendices 1 and 2. In addition, as shown in the Appendices 1 and 2, the effect of the strain on these distributions is not significant in the range of strains experienced by a typical myocardial tissue. Hence, these functions can be pre-computed before attempting to solve the finite element problem.

Finally, (22.5) can be expanded in terms of the distributions of the angles in the reference configuration. The equations for all six independent terms of the stress tensor look similar and are of the following form:

$$\begin{aligned} &\boldsymbol{T}_{\text{tissue}}(j,k) = S_{\text{f}}.F_{jk}\left(I_i(\gamma), \nu\right) \\ &\quad \text{where } i = \cos^2\gamma, \cos\gamma, \sin^2\gamma \quad \gamma = \beta, \varphi, \theta \end{aligned} \tag{22.7}$$

F_{jk} are pre-computable functions of the angle distributions. The actual form of these functions is given in the Appendices 1 and 2.

22.2.5 Simplifying Assumptions

In addition to the assumptions inherent to the construction of the model, a few additional simplifying assumptions were made. Because we have no detailed measurements of the angles φ and θ, these angles were replaced with a Von-Mises distribution centered about 0° with a fiber dispersion standard deviation of 12° (Karlon et al. 1998). This simplifies the resulting model due to the symmetry of these distributions, making the active stress tensor diagonal.

22.2.6 Finite Element Computational Model

The crossbridge and lattice models were derived analytically with MATLAB code utilizing a symbolic library. The resulting code was then implemented into the laboratory's custom finite element modeling environment (Continuity 6.3, www.continuity.ucsd.edu).

The active contraction in a continuum tissue was simulated with a nonlinear finite element model of a tissue slab. The chosen model includes passive material properties and a biophysically based tension generation. It is a 27-node, 8-element mesh of a tissue sample, which is synchronously activated.

Myocardial stresses are determined at each integration point within the finite element mesh by a summation of passive stress (due to distension) and active stress (due to crossbridge cycling). The passive stress model described by Guccione et al. (1991) is used as is. The active stresses are determined by the model described in the previous section.

To simulate equi-biaxial tests, the tissue was first activated to maximum active tension corresponding to the strong attachment of all crossbridges. This gives a new geometry where the passive stresses generated in the tissue are in equilibrium with the generated active stresses (Fig. 22.4). This geometry was then stretched equi-biaxially to generate curves similar to those reported by Lin and Yin (1998). Volume conservation was enforced using a semi-incompressible penalty formulation (Doll and Schweizerhof 2000).

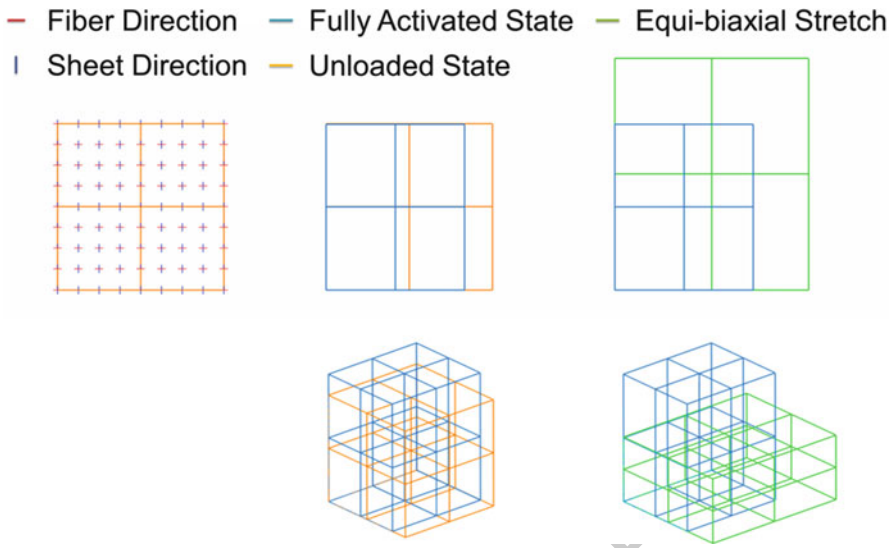

Fig. 22.4 Simulation of equi-biaxial stretch. The sample is first activated fully to obtain the geometry corresponding to the fully activated state (*middle*). The geometry is then stretched equally to simulate an equi-biaxial stretch

22.3 Results

22.3.1 Sheet Angle Measurements

Automated measurements of sheet angle were performed on 10 μm sections at every 1 mm depth through the ventricular wall (ten depths). Figure 22.5 shows an example of one section, as well as the results of the automated processing scheme, which was performed as described by Karlon et al. (1998). Results from the subendocardial and subepicardial regions are shown in Fig. 22.6. Note that there is substantial dispersion about the mean sheet angle ($\sigma > 10°$), particularly deeper in the wall.

For our simulations, we used the average dispersion data from these distributions. The average standard deviation of the dispersion is found to be about 30°. This corresponds to a concentration parameter (κ) value of 4 in the Von-Mises distribution. However, we did not include the bimodal distribution of sheets in our simulations since we were interested only in biaxial tests in isolated myocardial tissue.

22.3.2 Lattice Model

The effect of the lattice spacing on the transverse to fiber stress ratio was computed using the crossbridge and lattice model at typical lattice-spacing values (Julian et al.

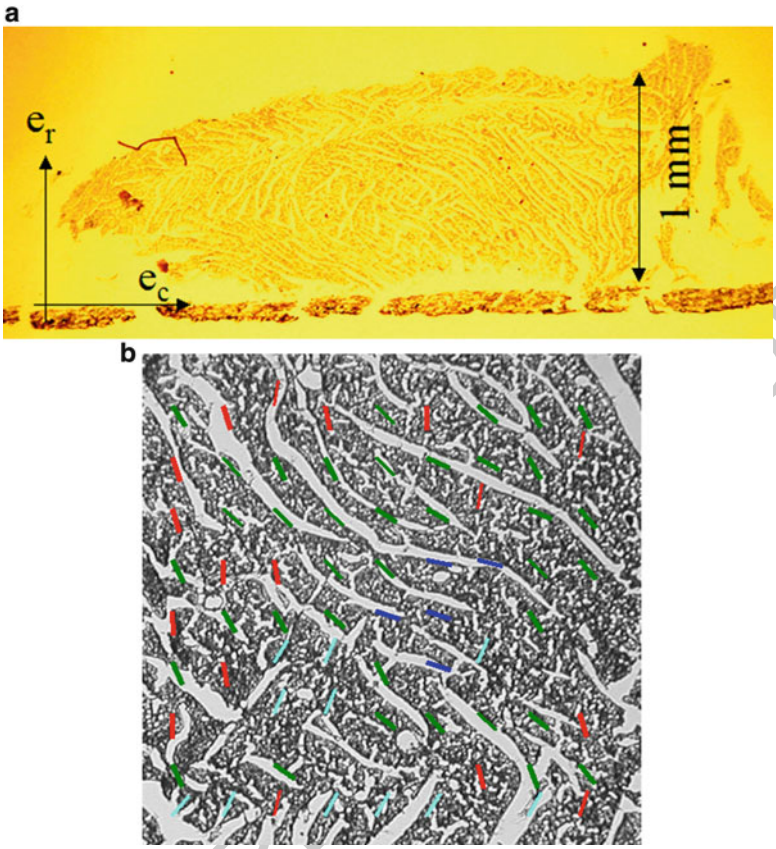

Fig. 22.5 Automated measurements of the sheet angle β. (**a**) 10 μm section of myocardium cut perpendicular to fiber angles. Gaps in tissue represent cleavage planes between myocardial sheets, which have opened up as tissue was allowed to desiccate for 10 min. In this image, two distinct populations of sheets are present. (**b**) Enlarged view of tissue section showing automated measurements of sheet angle. The region of interest for each measurement was 76 μm^2

1978; Schoenberg 1980a, b; Rayment et al. 1993). The lattice spacing is measured as the distance between adjacent actin and myosin filaments. The parameter values used for the crossbridge model are tabulated in Table 22.1. It can be seen that the radial to axial stress ratio is nonlinearly dependent on the lattice spacing.

It can be seen from Fig. 22.7 that this ratio of stresses depends on the length of the myosin S2 segment at lattice spacing corresponding to the unloaded sarcomere length. This length determines the angle the S2 segment makes with the myosin thick filament and hence in turn mediates the transverse force generated by the crossbridge.

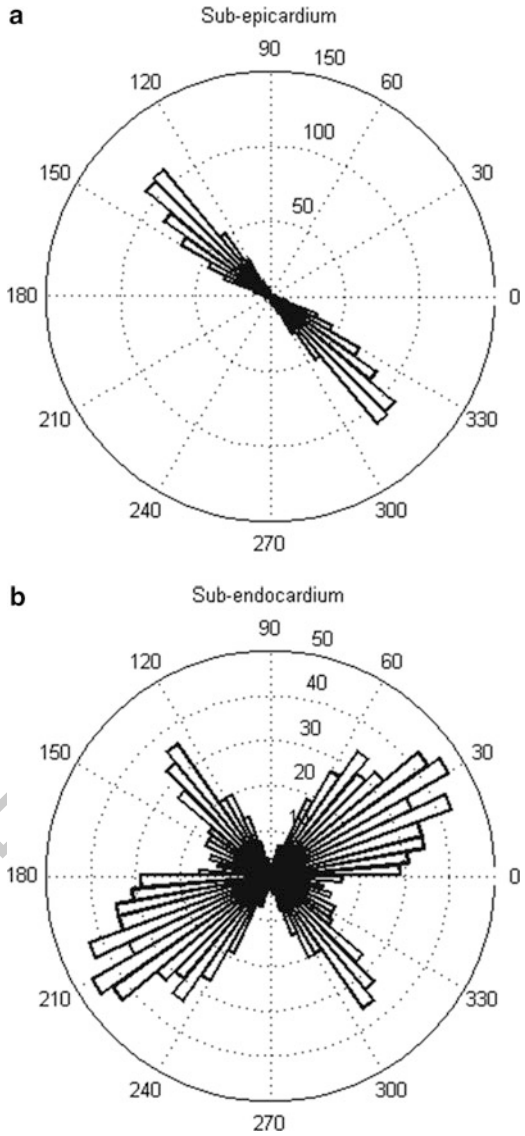

Fig. 22.6 Experimental distributions of the sheet angle β. Rose plots (circular histograms) showing the distribution of the sheet angle β in the sub-epicardium (**a**) and sub-endocardium (**b**). 0°/180° indicates that the sheet lie along the radial direction. It is clear that this animal has a second population of sheet angles in the sub-endocardium

22.3.3 Finite Element Model

The effect of fiber dispersion was tested using a finite element computational model of a rectangular slab of myocardium. The dimensions of the slab relative to the actual wall thickness of the heart are small such that sheet angle does not vary within the slab. The final form of the active stress-coupling model is given in the Appendices 1 and 2. Equi-biaxial stretch in a fully activated myocardial tissue was

Table 22.1 Parameter values for the crossbridge and lattice model

Parameter	Description	Value	Reference
l_0	Resting S2 segment length	12 nm	Williams et al. (2010)[a]
l_{S20}	S2 segment length at reference lattice spacing	16–20 nm	
l_{S1}	S1 segment length	11 nm	Schoenberg (1980a, b)[a]
α_{S1}	Angle of S1 attachment	45°	Julian et al. (1978)
δ_0	Axial distance of three myosin head pairs	43.5 nm	Craig and Woodhead (2006)
Δ_0	Lattice spacing at unloaded sarcomere length	19 nm	

[a]Values projected to 2D from a 3D model

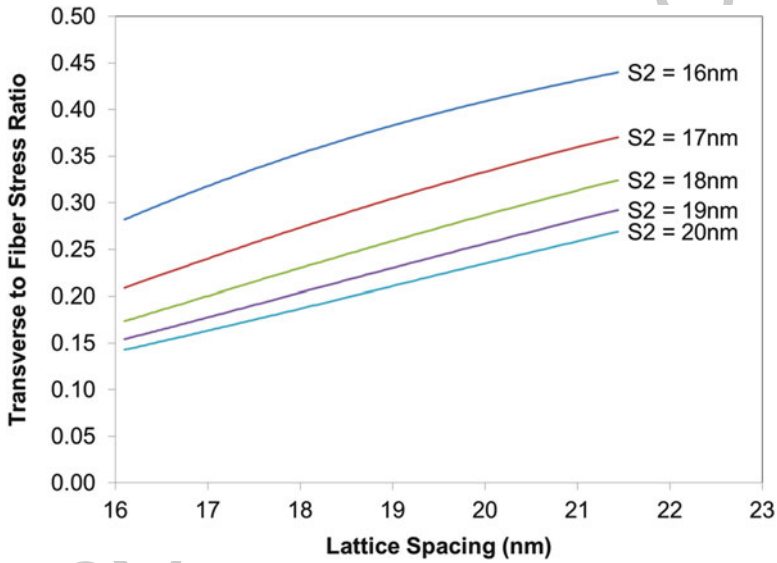

Fig. 22.7 Plot of the transverse to axial stress ratio as a function of lattice spacing between the actin and myosin filaments. This ratio is also a function of the length of the S2 myosin segment at reference lattice spacing as shown by the family of curves

simulated. Three simulations at sheet angles 0°, 45°, and 90° with respect to the second stretch direction were performed. Figure 22.8 shows the total stresses in the fiber and cross-fiber direction for the three sheet angles. It can be seen that the ratio of the cross-fiber to fiber stress varies depending on the sheet angle orientation. These may explain some of the variations in the experimental measurements by Lin and Yin (1998). In addition, this shows that the angle of the sheet relative to the applied stretch has a large effect on the total generated stress.

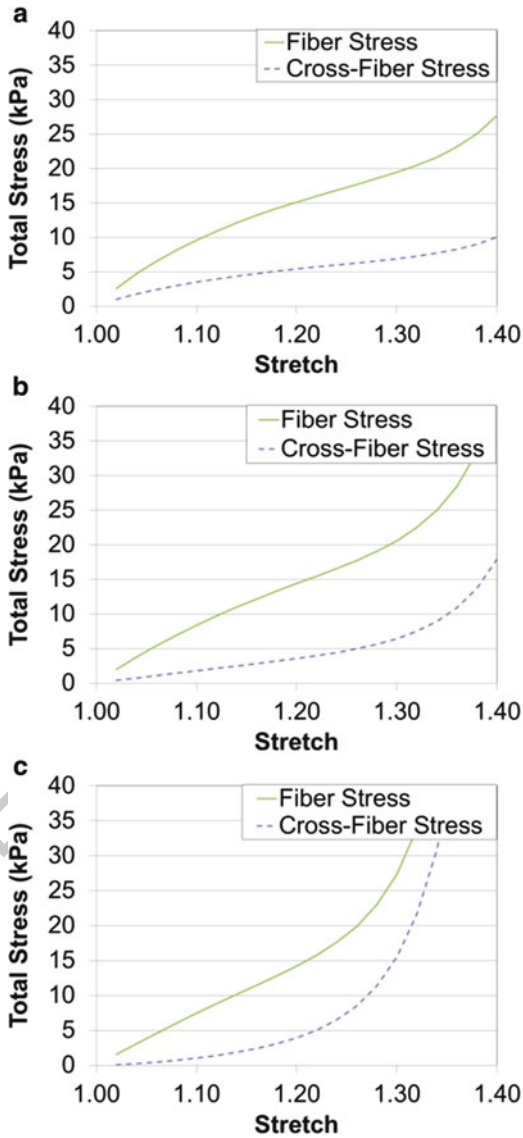

Fig. 22.8 Total fiber and cross-fiber stresses for three sheet angle orientations: 0° (**a**), 45° (**b**), and 90° (**c**). It can be seen that the ratio of the transverse to fiber stresses varies with the sheet angles

Figure 22.9 shows the active normal stresses generated in sheet coordinates as a function of the equi-biaxial stretch with the sheets parallel to the stretch plane. The experimental measurements given by Lin and Yin (1998) at one equi-biaxial stretch level are shown as points. It can be seen that on an average, the cross-fiber (sheet) stresses were around 40 % of the fiber stresses and the stresses in the sheet-normal direction were around 10 % of the fiber stresses. The active stress generated in the sheet-normal direction is only due to dispersion in the sheet angles.

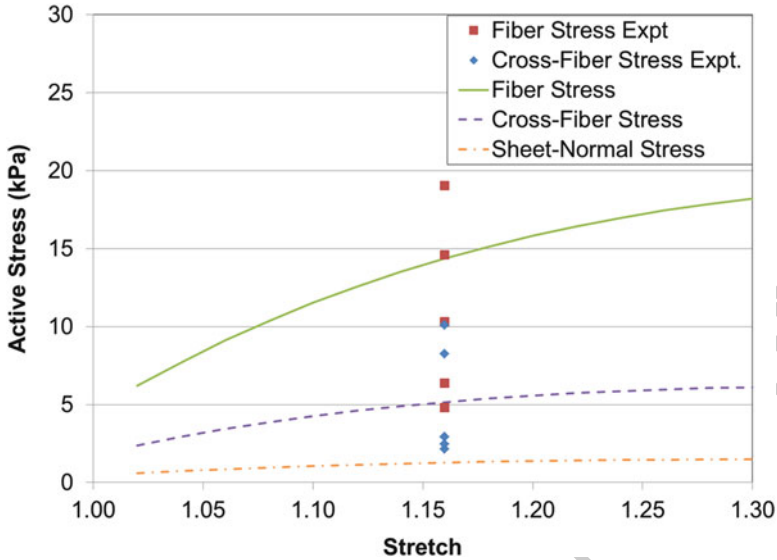

Fig. 22.9 Active fiber, cross-fiber, and sheet-normal stress generated in the tissue during equi-biaxial stretch. The experimental values from Lin and Yin (1998) at an equi-biaxial stretch of 1.16 are marked with *dots*

22.4 Discussion

In this study, we derive a multi-scale mathematical model to investigate the relationship between active force development within the sarcomere of a cardiac myocyte and stress transverse to the fiber orientation at the tissue level. The model incorporates structural dispersion including histological measurements of sheet orientation, and incorporates crossbridge and sarcomere lattice geometry. The results of the finite element model are compared with measured experimental stress in biaxial deformation tests. The results suggest that these mechanisms can explain the source of forces generated transverse to the fiber direction in myocardial tissue.

The transverse force generation in the crossbridge model is sensitive to the parameters of the model, such as the length of the S1 and S2 segments. While estimates for these quantities vary between publications and muscle types and species, they are measurable microstructural properties rather than arbitrary parameters.

Our analysis suggests that the strain dependence of fiber and sheet dispersion is very small and unlikely to affect the analysis. However, the strain dependence on lattice spacing gives rise to larger transverse stresses at larger lattice spacing. In the current model, we assume, based on electron microscopy and X-ray crystallography, that lattice spacing is only determined by fiber strain because the lattice isotropically expands in the transverse direction as sarcomeres shorten to maintain approximately constant sarcomere volume. This implies that anisotropic macroscopic strains in the myocardium must be accommodated either by rearrangement of myofibrils within myocytes, myocytes within sheets, or sheets within the tissue.

Since we consider the sheet to be a plane stress object, transverse stresses are not transmitted in the sheet-normal direction. The only mechanism of active stress generation in the sheet-normal direction in our model is through sheet dispersion. AQ4 This is probably not completely accurate since some form of inter-sheet coupling that can transmit active stresses in the sheet-normal direction. Myocardial sheets have also been shown to have unique passive material properties. For instance, they are stiffer within the plane of the sheet than across it (Dokos et al. 2002). Despite this, it has been shown that simulations of systole are insensitive to changes in parameters controlling passive sheet properties (Usyk et al. 2000).

In conclusion, we have developed a mathematical model linking scales from the myofilament crossbridge up to the tissue-scale myocardial continuum. The stress developed transverse to the myofilaments, in combination with dispersions of the muscle fibers and sheets, leads to significant transverse stress at the tissue level and found in previous experimental tests. The transverse active stress development in the tissue depends on structural geometry at multiple scales in the tissue. The orientation of the sheets relative to tissue deformation plays an important role in the total stress that is measured experimentally. The strain dependence of the transverse stress developed at the crossbridge level is significant while the strain dependence on the dispersion is found to be small as shown in the Appendices 1 and 2. Thus, we have developed a microstructurally based multi-scale model of active myocardial mechanics that takes into account the crossbridge and sarcomere lattice geometry and the myocardial sheet structure. Such a theoretical model can be easily incorporated into realistic ventricular geometry to simulate cardiac function that match closely with experimental observations.

Acknowledgement Supported by NIH grants 5P01HL46345, GM103426, 1R01HL96544, GM094503, 1RO1HL091036, and 1R01HL105242.

A.1 Appendix 1: Fiber-Sheet Dispersion Effects on Active Stress

Here we give details of the derivation of the fiber-sheet dispersion effects on active stress from (22.5). We used a Von-Mises distribution for the three angles. The probability density of a Von-Mises distribution is given by the following equation:

$$f(\gamma) = \frac{e^{\kappa \cos \gamma}}{2\pi I_0(\kappa)} \tag{22.8}$$

where I_0 is the modified Bessel function of order 0 and κ is called the concentration parameter that controls the standard deviation of the distribution. The components of the stress tensor can be computed to be

$$\begin{aligned}
\boldsymbol{T}_{11} &= S_{\mathrm{f}}\Big[\nu\left(I_{\sin^2\varphi}I_{\cos^2\theta} + I_{\cos^2\beta}I_{\cos^2\varphi}I_{\sin^2\theta}\right) \\
&\quad + \left(I_{\cos^2\varphi}I_{\cos^2\theta} + I_{\cos^2\beta}I_{\sin^2\varphi}I_{\sin^2\theta}\right)\Big] \\
\boldsymbol{T}_{22} &= S_{\mathrm{f}}\Big[\nu\left(I_{\sin^2\beta}I_{\cos^2\varphi}\right) + \left(I_{\sin^2\beta}I_{\sin^2\varphi}\right)\Big] \\
\boldsymbol{T}_{33} &= S_{\mathrm{f}}\Big[\nu\left(I_{\sin^2\varphi}I_{\sin^2\theta} + I_{\cos^2\beta}I_{\cos^2\varphi}I_{\cos^2\theta}\right) \\
&\quad + \left(I_{\cos^2\varphi}I_{\sin^2\theta} + I_{\cos^2\beta}I_{\sin^2\varphi}I_{\cos^2\theta}\right)\Big]
\end{aligned} \tag{22.9}$$

where the integrals I can be computed numerically from the distribution. For a standard dispersion of 12° for φ and θ, and a 30° for b, we get the active stress components to be given by

$$\begin{aligned}
\boldsymbol{T}_{11} &= S_{\mathrm{f}}\,[0.067\,\nu + 0.924] \\
\boldsymbol{T}_{22} &= S_{\mathrm{f}}\,[0.201\,\nu + 0.008] \\
\boldsymbol{T}_{33} &= S_{\mathrm{f}}\,[0.724\,\nu + 0.067]
\end{aligned} \tag{22.10}$$

These equations were then used in the finite element model and the k computed from the lattice model is used as the input to these models.

A.2 Appendix 2: Strain Dependence of Angle Distributions

In continuum mechanics, deformations of bodies create changes in angles. For example, consider the two-dimensional example in Fig. 22.10. Suppose the fibers in this tissue are originally oriented at an angle γ_0. After undergoing deformation, this angle is represented by γ. The relationship between γ and γ_0 can be derived from continuum mechanics principles (Fung 1993), and is given by:

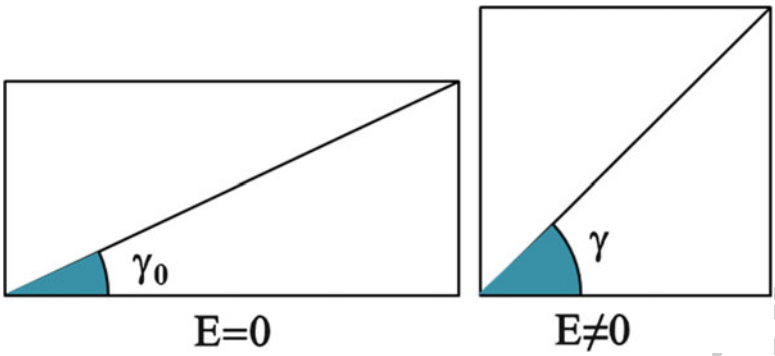

Fig. A.1 Schematic diagram representing the change in angle γ as a body deforms. In this example, due to horizontal shortening and vertical lengthening, $\gamma > \gamma_0$. The angle would also be affected by shearing deformation (*not shown*)

$$\begin{aligned}\cos\gamma &= \frac{\mathbf{u}_1\mathbf{C}\mathbf{u}_2}{\sqrt{\mathbf{u}_1\mathbf{C}\mathbf{u}_1}\sqrt{\mathbf{u}_2\mathbf{C}\mathbf{u}_2}} \\ &= \frac{\begin{bmatrix}1\\0\end{bmatrix}\begin{bmatrix}C_{11} & C_{12}\\ C_{12} & C_{22}\end{bmatrix}\begin{bmatrix}\cos\gamma_0\\ \sin\gamma_0\end{bmatrix}}{\sqrt{C_{11}}\sqrt{\begin{bmatrix}\cos\gamma_0\\ \sin\gamma_0\end{bmatrix}\begin{bmatrix}C_{11} & C_{12}\\ C_{12} & C_{22}\end{bmatrix}\begin{bmatrix}\cos\gamma_0\\ \sin\gamma_0\end{bmatrix}}} \\ &= \frac{C_{11}\cos\gamma_0 + C_{12}\sin\gamma_0}{\sqrt{C_{11}}\sqrt{C_{11}\cos^2\gamma_0 + 2C_{12}\sin\gamma_0\cos\gamma_0 + C_{22}\sin^2\gamma_0}}\end{aligned} \tag{22.11}$$

In terms of the strain components **E**, the $\cos(\gamma)$ can be computed from the equation,

$$\cos\gamma = \frac{(2E_{11}+1)\cos\gamma_0 + 2E_{12}\sin\gamma_0}{\sqrt{(2E_{11}+1)}\sqrt{\left(2E_{11}\cos^2\gamma_0 + 4E_{12}\sin\gamma_0\cos\gamma_0 + 2E_{22}\sin^2\gamma_0 + 1\right.}} \tag{22.12}$$

In order to understand the strain dependence of the fiber dispersion functions, several numerical experiments were performed. Samples of 5000 angles were drawn from a Von-Mises distribution of known κ, the concentration parameter, which gives a standard deviation of 12°. The change in the angle γ is computed for different values of biaxial strains, and the new standard deviation and the κ parameter were computed for the resulting distribution (Fig. 22.11). This was then compared with directly computing the change in the standard deviation angle using (22.12). It can

AQ5

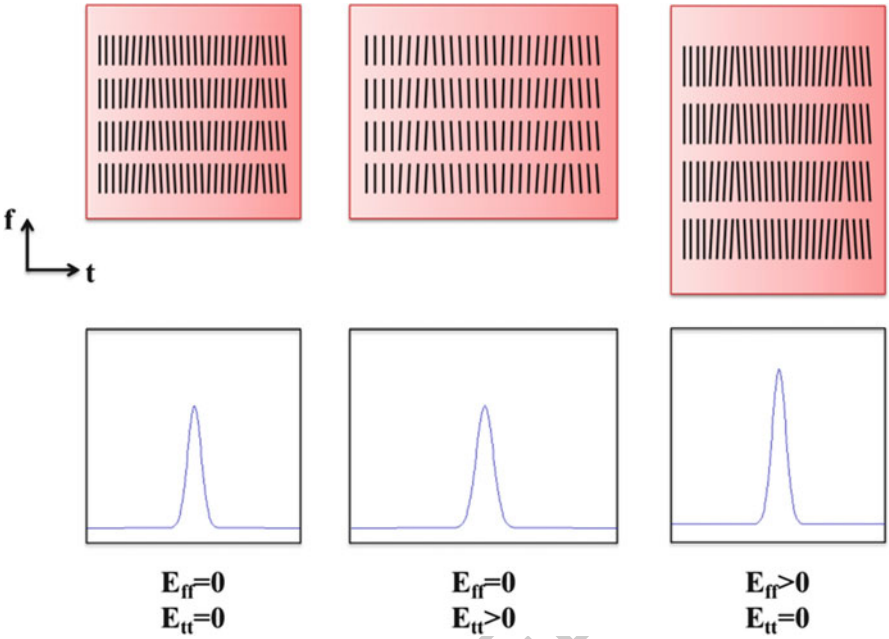

Fig. A.2 Effect of strain on fiber distribution. A positive transverse strain increases the standard deviation of the angle distribution while a positive fiber strain decreases the standard deviation

be seen from Fig. 22.12 that the predicted standard deviations are within few degrees of the predicted values. Under shear strain, the mean is not zero, but this deviation in the mean is <2° for reasonable shear strains.

Next, the strain dependence of the active stress components was computed (Fig. 22.13). The concentration parameter was varied from 10 to 40 for φ and θ, and from 2 to 10 for the sheet angle β. These correspond to a standard deviation of 18°–9° for φ and θ, and 48°–18° for β, respectively. It can be seen from Fig. 22.14 that the strain dependence is very small for practical values of standard deviation of fiber dispersion and strains. Consequently, the strain dependence can be ignored for typical strains in a myocardium. In addition, if the strain values are extreme, the strain dependence can be incorporated by computing the new standard deviation of the distribution and using the concentration parameter that corresponds to this standard deviation value in the simulations.

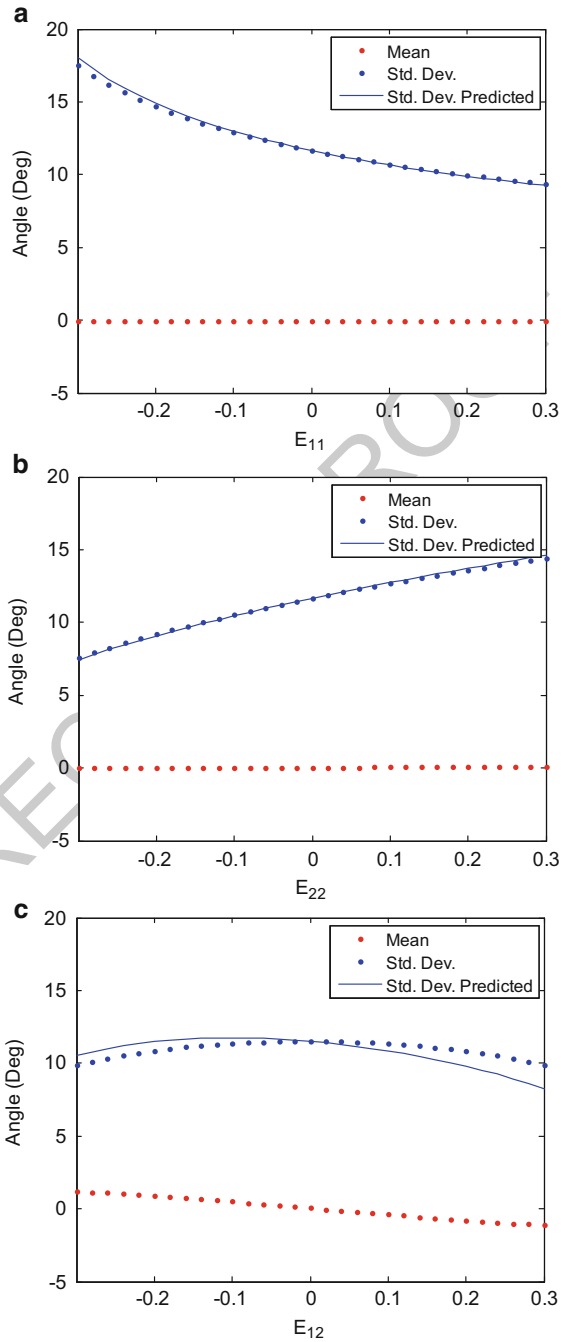

Fig. A.3 Comparison of actual standard deviation with predicted values for different strains

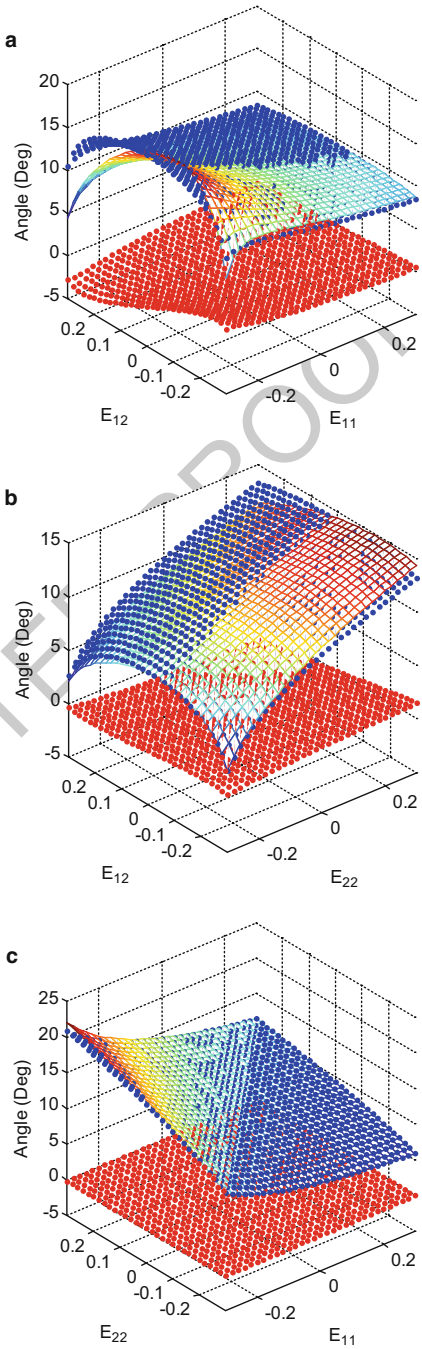

Fig. A.4 Effect of combined biaxial strains on standard deviation and its prediction

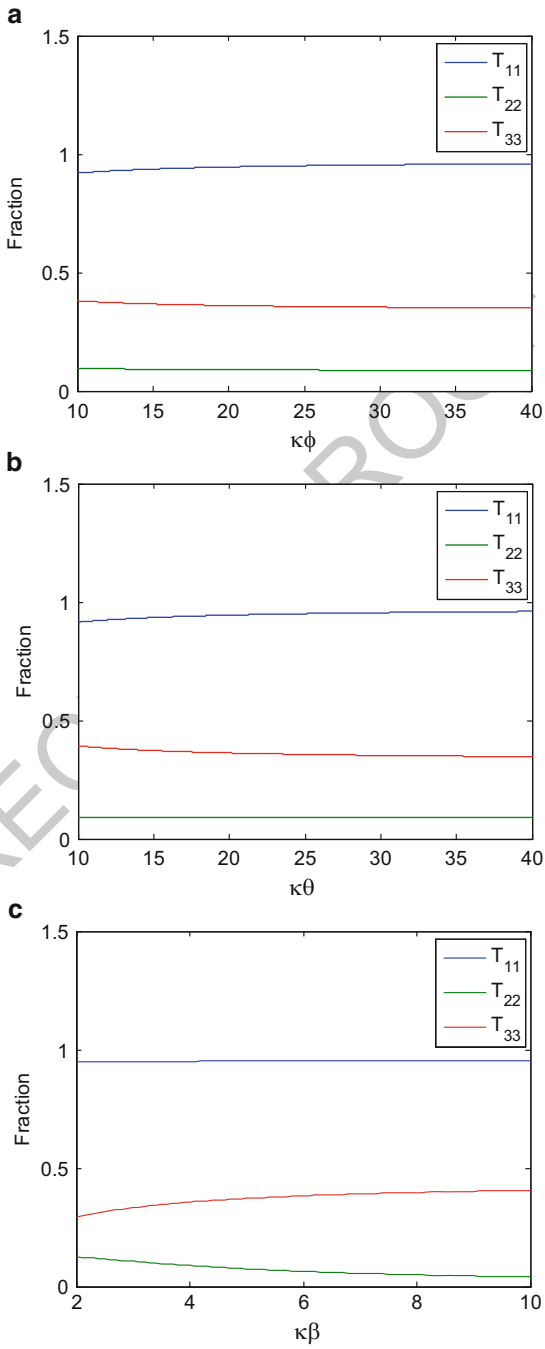

Fig. A.5 Effect of the concentration parameter κ on the diagonal components of the active stress tensor. It can be seen that the strain dependence is very small and we can ignore it for practical simulations

References

Ashikaga H, Omens JH, et al. Transmural mechanics at left ventricular epicardial pacing site. Am J Physiol Heart Circ Physiol. 2004;286:H2401–7.

Campbell SG, Howard E, et al. Effect of transmurally heterogeneous myocyte excitation-contraction coupling on canine left ventricular electromechanics. Exp Physiol. 2009;94: 541–52.

Campbell SG, Lionetti FV, et al. Coupling of adjacent tropomyosins enhances cross-bridge-mediated cooperative activation in a Markov model of the cardiac thin filament. Biophys J. 2010;98:2254–64.

AQ6 Chuang JS, Tangney JR, et al. Novel role for vinculin in myocardial fiber mechanics and heart failure. Circ Res. 2012.

Coppola BA, Covell JW, et al. Asynchrony of ventricular activation affects magnitude and timing of fiber stretch in late-activated regions of the canine heart. Am J Physiol Heart Circ Physiol. 2007;293:H754–61.

Costa KD, Takayama Y, et al. Laminar architecture and three-dimensional systolic mechanics in canine ventricular myocardium. Am J Physiol. 1999;276:H595–607.

Craig R, Woodhead JL. Structure and function of myosin filaments. Curr Opin Struct Biol. 2006;16(2):204–12.

Dokos S, Smaill BH, et al. Shear properties of passive ventricular myocardium. Am J Physiol Heart Circ Physiol. 2002;283:2650–9.

Doll S, Schweizerhof K. On the development of volumetric strain energy functions. J Appl Mech. 2000;67:17.

Fung YC. A first course in continuum mechanics. Englewood Cliffs: Prentice-Hall; 1993.

Guccione JM, McCulloch AD. Mechanics of active contraction in cardiac muscle: Part I—constitutive relations for fiber stress that describe deactivation. J Biomech Eng. 1993;115: 72–81.

Guccione JM, McCulloch AD, et al. Passive material properties of intact ventricular myocardium determined from a cylindrical model. J Biomech Eng. 1991;113:42–55.

Hunter PJ, McCulloch AD, et al. Modelling the mechanical properties of cardiac muscle. Prog Biophys Mol Biol. 1998;69(2/3):289–331.

Huxley HE. The crossbridge mechanism of muscular contraction and its implications. J Exp Biol. 1985;115:17–30.

Huxley HE, Kress M. Crossbridge behaviour during muscle contraction. J Muscle Res Cell Motil. 1985;6(2):153–61.

Julian FJ, Moss RL, et al. The mechanism for vertebrate striated muscle contraction. Circ Res. 1978;42(1):2–14.

Karlon WJ, Covell JW, et al. Automated measurement of myofiber disarray in transgenic mice with ventricular expression of ras. Anat Rec. 1998;252(4):612–25.

LeGrice IJ, Smaill BH, et al. Laminar structure of the heart: ventricular myocyte arrangement and connective tissue architecture in the dog. Am J Physiol. 1995;269:H571–82.

Lin DH, Yin FC. A multiaxial constitutive law for mammalian left ventricular myocardium in steady-state barium contracture or tetanus. J Biomech Eng. 1998;120(4):504–17.

Rayment I, Holden HM, et al. Structure of the actin-myosin complex and its implications for muscle contraction. Science. 1993;261(5117):58–65.

Schoenberg M. Geometrical factors influencing muscle force development. I. The effect of filament spacing upon axial forces. Biophys J. 1980a;30(1):51–67.

Schoenberg M. Geometrical factors influencing muscle force development. II. Radial forces. Biophys J. 1980b;30:69–77.

Usyk TP, Mazhari R, et al. Effect of laminar orthotropic myofiber architecture on regional stress and strain in the canine left ventricle. J Elas. 2000;61:143–64.

Williams CD, Regnier M, et al. Axial and radial forces of cross-bridges depend on lattice spacing. PLoS Comput Biol. 2010;6(12):e1001018.

Zahalak GI. Non-axial muscle stress and stiffness. J Theor Biol. 1996;182:59–84.

AUTHOR QUERIES

AQ1. Please provide email address for the corresponding author.
AQ2. Schoenberg 1980 has been changed to Schoenberg 1980a, 1980b as per the reference list in similar occurrences. Please check if okay.
AQ3. Appendix has been changed to Appendices 1 and 2. Please check.
AQ4. Please check the edit made in the following sentence:"This is probably not completely . . . "
AQ5. Please check for the missing inserted citation for Figs. 22.11 and 22.13.
AQ6. Please provide volume and page range for reference "Chuang et al. 2012".